

Check for updates

# Holistic Recovery of Spent Lithium-Ion Batteries by Flash Joule Heating

Shichen Xu, Justin Sharp, Qiming Liu, Jaeho Shin, Haoxin Ye, Kaiwen Yang, Shihui Chen, Karla Silva, Ralph Abdel Nour, Carter Kittrell, Haojie Zhu, Bowen Li, Khalil JeBailey, Carolyn Teng, Boris I. Yakobson, Yufeng Zhao,\* and James M. Tour\*

The rising demand for lithium-ion batteries (LIBs) highlights the urgent need for sustainable recycling technologies. Existing pyrometallurgy and hydrometallurgy methods can recover valuable metals but suffer from high energy costs and wastewater generation. Here, a selective flash Joule heating chlorination and oxidation (FJH-ClO) strategy is presented for the efficient separation of metals from spent batteries. In this process, cathode metals are first chlorinated for 60 s, after which the transition metal chlorides are oxidized to oxides, enabling lithium to be separated from transition metals due to their different aqueous solubility. This approach applies not only to the recovery of metals from lithium cobalt oxide (LCO), lithium iron phosphate (LFP), and lithium manganese iron phosphate (LMFP) cathode materials, but also to the anodic graphite, all from the black mass. The recovered graphite exhibits purity of ≈100% with a yield of 85%, Co at 99% purity and 97% yield, and Li at 99% purity with a 92% yield. Gram-scale experiments confirm the scalability of the method, maintaining high efficiency and selectivity. Life-cycle assessment and technoeconomic analysis reveal that the FJH-CIO process substantially reduces energy consumption, operation time, and reagent consumption, while lowering operating costs by up to 92%, compared to conventional approaches.

S. Xu, J. Sharp, Q. Liu, J. Shin, H. Ye, K. Yang, S. Chen, K. Silva, C. Kittrell, H. Zhu, B. Li, C. Teng, J. M. Tour

Department of Chemistry

Rice University

Houston, TX 77005, USA E-mail: tour@rice.edu

R. A. Nour, J. M. Tour

Applied Physics Program and Smalley-Curl Institute

Rice University

Houston, TX 77005, USA

K. JeBailey, B. I. Yakobson, Y. Zhao, J. M. Tour

Department of Materials Science and NanoEngineering

Rice University

Houston, TX 77005, USA

E-mail: YZhao@corban.edu

Y. Zhao

Department of Physics

Corban University

5000 Deer Park Drive SE, Salem, OR 97317, USA

J. M. Tou

NanoCarbon Center and the Rice Advanced Materials Institute Rice University

Houston, TX 77005, USA

The ORCID identification number(s) for the author(s) of this article can be found under https://doi.org/10.1002/adma.202517293

DOI: 10.1002/adma.202517293

#### 1. Introduction

The rapid advancement of industrial automation and the innovation of portable electronic devices have driven the growth of the lithium-ion battery (LIB) market.[1-6] LIBs have broad applications, ranging from electric vehicles and warehouse logistics equipment to wearable devices and smartphones, which benefit from their high energy density, fast charging capability, and long cycle life.[2,7,8] The widespread use of electronic products based on LIBs results in large quantities of discarded batteries.[7,9,10] Current predictions for the global market of spent LIB metals estimate it will reach nearly \$22.8 billion by 2030, with a compound annual growth rate of ≈20%.[4,11,12] A closed-loop recovery method for critical metals, particularly lithium (Li), from cathode waste through urban mining is essential for preventing supply chain disruptions.[3,6,13-15] This approach diminishes the need for traditional mining of

battery metals, reduces the environmental consequences of waste removal and traditional mining, and economically incentivizes recycling to promote a circular economy.<sup>[13,16]</sup>

Recycling the cathode from spent LIBs is especially important due to the presence of high-value precious metals and residual Li, and achieving an efficient separation between them is especially critical for developing closed-loop battery recycling systems. [13,17-20] Conventional methods for the separation of cathode metals include hydrometallurgical, pyrometallurgical, and electrochemical strategies.[1,4,5,9,21] Hydrometallurgy, which involves acid leaching and subsequent solvent extraction or precipitation, offers improved energy efficiency while enabling highly selective Li separation.[22-29] Nonetheless, it often requires extensive leaching duration and large volumes of concentrated acid while generating secondary wastewater (Figure 1a, left).[22-28] Pyrometallurgy features simplified treatment and demonstrates strong versatility in handling different cathode materials.[30-36] However, high energy consumption during high-temperature smelting increases costs (Figure 1a, middle).[30-36] Electrochemical Li separation from spent electrodes offers high selectivity and mild operating conditions.[37-41] However, this method suffers from slow kinetics and limited scalability.[38-40] Thus, exploiting

//advanced.onlinelibrary.wiley

om/doi/10.1002/adma.202517293 by James M Tour - Rice University , Wiley Online Library on [15/11/2025]. See the Terms

on Wiley Online Library for rules of use; OA articles are governed by the applicable Creative Commons

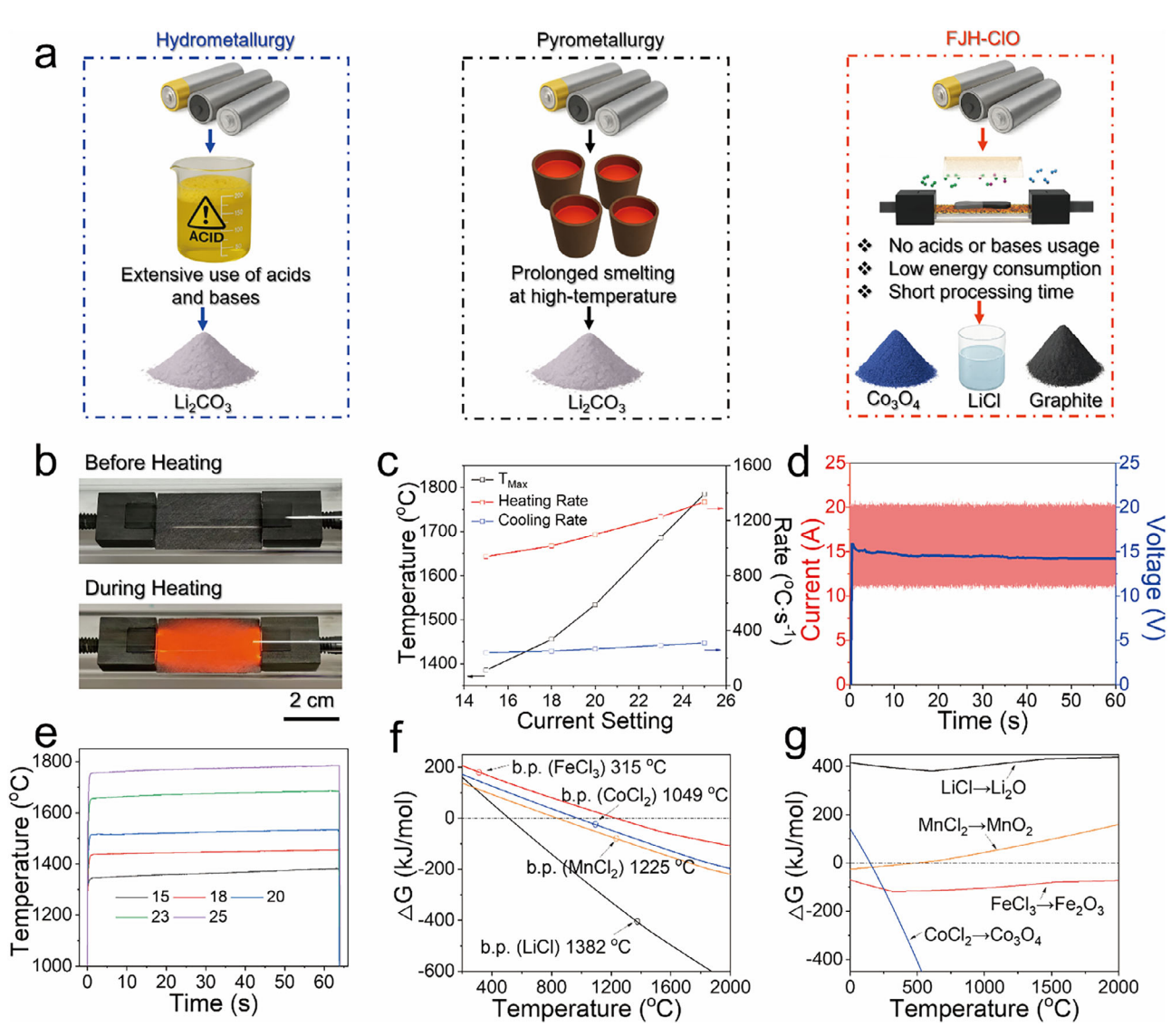


Figure 1. Flash Joule heating method for metal extraction and thermodynamic analysis. a) Schematic illustration of Li separation via hydrometallurgy, pyrometallurgy, and FJH(ClO) processes. b) Pictures of carbon paper before (top) and during (below) Joule heating. c) Heating and cooling rates under different current settings. d) Current and voltage changes during Joule heating at a current setting of 15. e) Temperature vs time profiles under different current settings. f) Thermodynamic calculation results for the chlorination of active materials (LCO, LFP, and LMFP) in a battery. g) Thermodynamic calculation results for the oxidation of LiCl, CoCl<sub>2</sub>, FeCl<sub>3</sub>, and MnCl<sub>2</sub>.

efficient and environmentally friendly Li separation technology is crucial for promoting sustainable battery recycling.

Flash Joule heating (FJH), as a rapid heating technique, has found applications beyond diverse materials synthesis, [42–44] particularly in metal recovery from electronic waste (e-waste). [45–48] Unlike our previous pulsed FJH-chlorination system powered by a capacitor bank, [48] which required repeated charging-discharging cycles and offered limited temperature stability, the present work employs a continuous DC-powered FJH setup enabling uniform, precisely controlled heating. Moreover, single-step chlorination was effective for metals with large thermodynamic differences (e.g., Ga, In, Ta); however, the single-step chlorination is insufficient for separating Li from transition metals. Here, a two-step process comprising FJH chlorination and oxidation (FJH-ClO) is employed to selectively convert battery metals

into chlorides and oxides, respectively, allowing for the separation of Li from other metals based on their differential aqueous solubility (Figure 1a, right). While chlorination is fundamentally an oxidation step, we distinguish that here from an air oxidation step, which generates metal oxides. FJH-chlorination of LCO with  $\text{Cl}_2$  gas for 60 s can convert both Li and Co into their corresponding chlorides. Subsequent oxidation in air at 450 °C transforms  $\text{CoCl}_2$  into cobalt oxides, predominantly  $\text{Co}_3\text{O}_4$ , while LiCl remains unoxidized, which allows for effective separation of Li from Co during a water leaching step because of the high solubility of LiCl, achieving a Li purity of >99% and a recovery rate of 92%. This strategy can be extended to other cathode materials such as LiFePO $_4$  (LFP) and LiMnFePO $_4$  (LMFP), as well as to complex feedstocks like mixed cathode waste and black mass. When applied to the black mass, the efficient separation of Li,

15214055, O. Downloaded from https://advanced.onlinelibrays.wiley.com/doi/10.102/adma.2025/7293 by James M Tour - Ric University, Wiley Online Library on [15/11/2025]. See the Terms and Conditions (https://onlinelibrary.wiley.com/erms-and-conditions) on Wiley Online Library for rules of use; OA articles are governed by the applicable Creative Commons Licenses are Conditions on Wiley Online Library for rules of use; OA articles are governed by the applicable Creative Commons Licenses are Conditions on Wiley Online Library for rules of use; OA articles are governed by the applicable Creative Commons Licenses are conditions on Wiley Online Library for rules of use; OA articles are governed by the applicable Creative Commons Licenses are conditions of the Creative Commons Licenses are conditions on Wiley Online Library for rules of use; OA articles are governed by the applicable Creative Commons Licenses are conditions of the Creati

valuable metals such as Co, and graphite can be realized, providing a feasible approach for the well-managed recovery of end-of-life LIBs. By avoiding prolonged high-temperature smelting and acid leaching, this method offers a low-energy, low-cost, acid-free, and environmentally friendly alternative to traditional pyrometallurgical and hydrometallurgical processes.

# 2. Thermodynamic Analysis of Lithium Separation in a Flash Joule Heating System

In our flash Joule heating system, a direct current power supply (DCPS) is connected via electrodes to carbon paper assembled with graphite blocks (Figure S1, Supporting Information), and the carbon paper can be rapidly heated to over 1000 °C, with its surface glowing orange-red (Figure 1b). By adjusting the DCPS dial to regulate the current setting, the temperature of the carbon paper during resistive heating can be precisely controlled (Figure 1c). For instance, when the current setting is 15, the temperature reaches ≈1385 °C; increasing the current setting to 18 raises the temperature to ≈1455 °C. As the current increases, the heating rate correspondingly accelerates (Figure 1c; Table S1, Supporting Information). Once the power is turned off, the temperature of the carbon paper drops below 1000 °C within milliseconds (Figure S2, Supporting Information). Importantly, the heating process is stable with consistently steady voltage, despite small periodic variations in current (Figure 1d), enabling the carbon paper to maintain temperatures above 1000 °C for more than 60 s (Figure 1e; Figure S3, Supporting Information). The excellent temperature stability and precise controllability of the FJH process ensure the reliability, reproducibility, and overall consistency of the experimental results. The slight variations of temperature observed are primarily attributed to minor changes in the resistance of carbon paper during heating. The dial setting on the DCPS is a relative current setting, but that has been calibrated (Table S2, Supporting Information).

A thermodynamic analysis shows that the chlorination of Li occurs at a temperature higher than 514 °C, where the Gibbs free energy is negative ( $\Delta G < 0$ ) (Figure 1f; Table S3, Supporting Information). But LiCl has a high boiling point of 1382 °C. The temperatures for the chlorination of Co in LCO, Fe in LFP and LMFP, and Mn in LMFP are 990, 1230, and 840 °C, respectively, which are all higher than that for Li (Figure 1g; Table S3, Supporting Information). The boiling points of CoCl<sub>2</sub>, FeCl<sub>3</sub>, and MnCl<sub>2</sub> are 1049, 315, and 1225 °C, respectively, which are lower than that of LiCl (Table \$3, Supporting Information). Though one-step chlorination is challenging to separate Li from other cathode metals, all the metal chlorides can be collected after the chlorination happens at a temperature higher than the boiling point of LiCl (1382 °C). Considering the different temperatures for the oxidation of LiCl and other cathode metal chlorides, oxidation of CoCl<sub>2</sub>, FeCl<sub>3</sub>, and MnCl<sub>2</sub> can operate when the temperature is 450 °C, while the oxidation of LiCl is not favored between 0 and 2000 °C, even the molar ratio of O<sub>2</sub> to LiCl is 100:1 (Figure 1g; Figure S4, and Table S4, Supporting Information). Benefiting from the high solubility of LiCl in water (42.6 g/100 mL at 20 °C), Li can be efficiently separated from other metal oxides via a one-step water leaching process.

# 3. Li Separation from Cathode Active Materials: LCO, LFP, and LMFP

The conceptual diagram is shown in detail in Figure 2a, where Li and other battery metals undergo chemical phase transformations through FIH chlorination followed by oxidation in air (FIH-ClO) treatment, enabling their separation based on solubility differences. LiCoO2 (LCO) is one of the most used cathode active materials in LIBs, making Li recover from LCO exemplary. The study commenced with the chlorination of LCO powder (Figure S5, Supporting Information). The particle size is 5–20 µm, and the inductively coupled plasma mass spectrometry (ICP-MS) results show that the initial LCO contains 10.5% Li and 89.5% Co (Figure S6, Supporting Information). When the dial of the DCPS was set at 18 (≈1455 °C), pink and blue powders formed and deposited on the quartz tube during the first-step chlorination, exhibiting colors consistent with those of CoCl2 and its hydrate (Figure 2b, upper inset). After 60 s of exposure to Cl<sub>2</sub> gas at the temperature, only negligible amounts of residual LCO powder were observed on the carbon paper (Figure \$7, Supporting Information), indicating that almost all metallic components had been chlorinated and subsequently evaporated and deposited onto the surface of the quartz tube, which was referred to as the volatile phase. Carbon felts and glass wool were used to lightly restrict the outlet of the quartz tube for better collection of volatiles (Figure S8, Supporting Information). A further elemental analysis by energy dispersive X-ray spectroscopy (EDS) revealed that the pristine material primarily contained Co and O (Figure 2b, bottom), and Li was undetectable due to its low characteristic X-ray energy. In contrast, the volatile phase predominantly contained Cl and Co after chlorination, suggesting a successful conversion from LCO to chlorides (Figure 2b, top). X-ray diffraction (XRD) patterns further confirmed the occurrence of the chlorination reaction. The initial material corresponded to the LiCoO<sub>2</sub> phase, while the volatile phase exhibited peaks corresponding to LiCl·H<sub>2</sub>O and CoCl<sub>2</sub>·2H<sub>2</sub>O (Figure 2c). Because of the strong hygroscopic nature of both LiCl and CoCl<sub>2</sub>, the formation of hydrates occurs upon exposure to ambient moisture. This moisture-induced hydration also explains the observed blue and pink color of the deposits on the tube wall (Figure 2b, top inset). Additionally, X-ray photoelectron spectroscopy (XPS) analysis further corroborates the successful chlorination process (Figure 2d-f; Figure S9, Supporting Information). In the pristine LCO, no Cl 2p signal is detected (Figure 2d, bottom), while a clear Li 1s peak is observed at 54.23 eV (Figure 2e, bottom), corresponding to Li metal species, and the Co 2p region exhibits typical features of Co<sup>3+</sup> in LiCoO<sub>2</sub> (Figure 2f). After chlorination, a strong Cl 2p signal appears at 198.57 eV (Figure 2d, middle), confirming the formation of LiCl and CoCl<sub>2</sub>. The Li 1s peak remains but slightly shifts to 56.02 eV (Figure 2e, middle), indicating a change in chemical environment from LiCoO $_2$  to LiCl. The Co  $2p_{3/2}$  spectrum exhibits characteristic changes corresponding to the valence state transition from Co<sup>3+</sup> in LiCoO<sub>2</sub> to Co<sup>2+</sup> in CoCl<sub>2</sub>, including a shift of the main peak (779.41 eV) toward higher binding energy (781.03 eV) and the emergence of pronounced satellite peaks (purple color), both of which are indicative of the change in cobalt oxidation state (Figure 2f, middle).

Following the oxidation process in air at 450  $^{\circ}$ C for 30 min, the Cl 2p signal and Li 1s peak persist due to the stability of LiCl

810

800

790

Binding energy (eV)

780

770

15214095, 0, Downloaded from https://advanced.onlinelibrary.wiley.com/doi/10.1002/adma.2025/17293 by James M Tour - Rice University , Wiley Online Library on [15/11/2025]. See the Terms and Conditions (https://onlinelibrary.wiley

litions) on Wiley Online Library for rules of use; OA articles are governed by the applicable Creative Commons

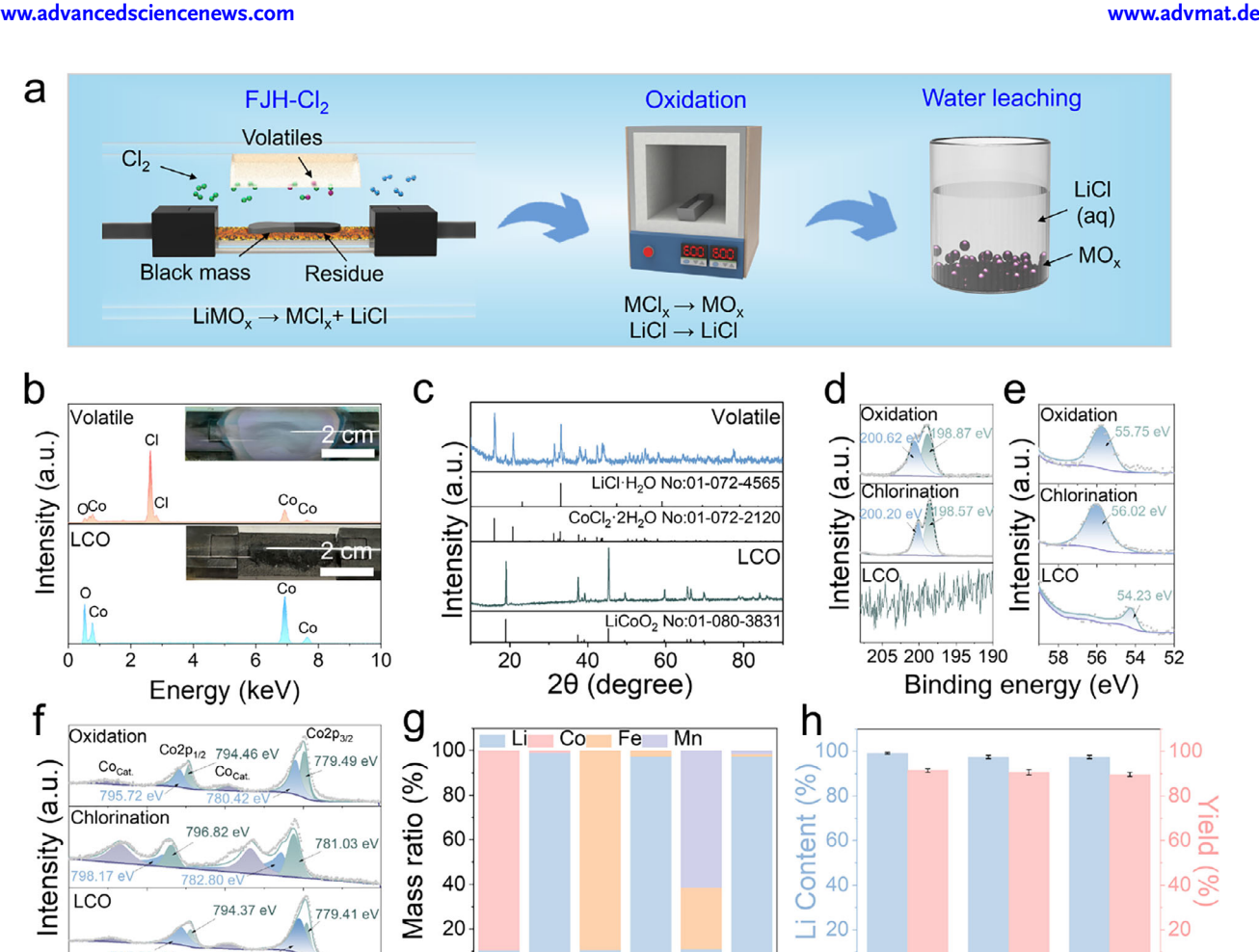


Figure 2. Li separation from LCO, LFP, and LMFP cathode powder. a) Schematic diagram of Li and transition metal separation via chlorination-oxidationwater leaching process. b) SEM-EDS analysis of raw LCO (bottom) and volatile (top) after chlorination. Insets are the photos of the quartz tube before (bottom) and after (top) chlorination. c) XRD patterns of raw LCO (bottom) and the volatile (top) after chlorination. The PDF card numbers are noted with the referenced spectral lines. d) Cl 1s, e) Li 1s, and f) Co 2p XPS signals in raw LCO powder (bottom), chlorinated powder (middle), and oxidized powder (top). g) Element mass percentage in raw cathode powder (LCO, LFM, LMFP) and separated samples. h) Content (blue) and yield (purple) of Li after separation from three different cathode materials. All error bars in (g,h) represent the standard deviation, where N=3.

Raw After Raw After Raw After

LFP

**LMFP** 

0

LCO

(Figure 2d,e, top), whereas the Co 2p spectrum evolves into a pattern characteristic of Co<sub>3</sub>O<sub>4</sub> with a mixed oxidation state of Co<sup>3+</sup> and Co<sup>2+</sup>, indicating the successful oxidation of CoCl<sub>2</sub> (Figure 2f), which is also confirmed by the XRD results (Figure \$10, Supporting Information). These results demonstrate that chlorination converts the LCO into volatile chlorides, and subsequent oxidation selectively reverts Co into its oxide form while preserving Li as the chloride. The oxidized samples were gently stirred in 10 mL of water and left to stand for 3 h. The suspension was then centrifuged for 5 min, and the supernatant was collected with a syringe and passed through a 22 µm syringe filter into another centrifuge tube, diluted, and prepared for analysis. The inductively coupled plasma mass spectrometry (ICP-MS) results show that the Li content increased from 10.5% in the initial LCO to 99.2% after undergoing the FJH-ClO and water leaching process. Moreover, the Li recovery rate is highly dependent on the temperature of the first-step chlorination reaction. Increasing the reaction temperature from 1385 to 1455 °C enhances the recovery rate from 43.3% to 91.5% (Figure S11, Supporting Information). Meanwhile, the valuable Co was also successfully separated and recovered, with a purity of 99.7% and a yield of 96.2% (Figure \$12, Supporting Information). This method is also extended to the Li separation from LFP powder (Figures S13-S16, Supporting Information). Li was also cleanly separated and recovered from LFP, achieving a Li purity of 97.4% and a yield of 90.7% for LFP (Figure \$17, Supporting Information). Li can also be separated and recovered from LMFP with a Li purity of 97.4% and a yield of 89.6% (Figures S18-S22, Supporting Information).

LCO

LFP

Cathode type

LMFP

# 4. Li Separation from the Cathode Waste and Black Mass

In addition to recovering Li from cathode powders, this method can also be applied to separate and recover Li, Co, and graphite

15214095, 0, Downloaded from https://advanced.onlinelibrary.wiley.com/doi/10.1002/adma.202517293 by James M Tour - Rice University , Wiley Online Library on [15/11/2025]. See the Terms and Conditions (https://advanced.onlinelibrary.wiley.com/doi/10.1002/adma.202517293 by James M Tour - Rice University , Wiley Online Library on [15/11/2025]. See the Terms and Conditions (https://advanced.onlinelibrary.wiley.com/doi/10.1002/adma.202517293 by James M Tour - Rice University , Wiley Online Library on [15/11/2025]. See the Terms and Conditions (https://advanced.onlinelibrary.wiley.com/doi/10.1002/adma.202517293 by James M Tour - Rice University , Wiley Online Library on [15/11/2025]. See the Terms and Conditions (https://advanced.onlinelibrary.wiley.com/doi/10.1002/adma.202517293 by James M Tour - Rice University , Wiley Online Library on [15/11/2025]. See the Terms and Conditions (https://advanced.onlinelibrary.wiley.com/doi/10.1002/adma.202517293 by James M Tour - Rice University , Wiley Online Library on [15/11/2025]. See the Terms and Conditions (https://advanced.onlinelibrary.wiley.com/doi/10.1002/adma.202517293 by James M Tour - Rice University , Wiley Online Library on [15/11/2025]. See the Terms and Conditions (https://adma.202517293 by James M Tour - Rice University , Wiley Online Library on [15/11/2025]. See the Terms and Conditions (https://adma.202517293 by James M Tour - Rice University ).

ions) on Wiley Online Library for rules of use; OA articles are governed by the applicable Creative Commons

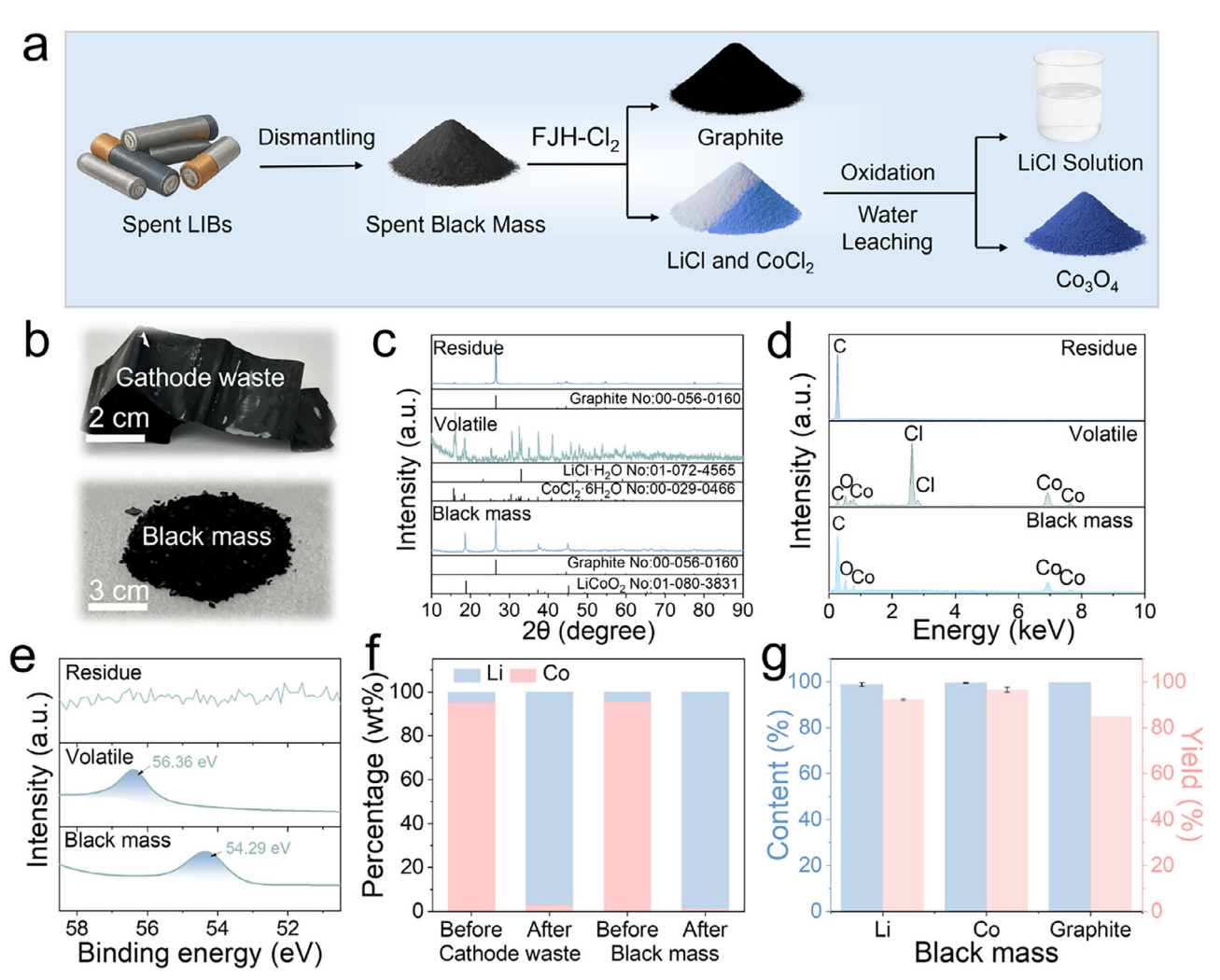


Figure 3. Li separation from LCO-based black mass. a) Schematic diagram of the separation of lithium, cobalt, and graphite from carbon black. b) Photo of the LCO cathode waste (upper) and black mass (below). c) XRD patterns of raw black mass (bottom), chlorinated powder (middle), and residue (top). d) SEM-EDS elemental analysis of raw black mass (bottom), volatile (middle), and residue (below) after chlorination. e) XPS of Li 1s in raw black mass (bottom), volatile (middle), and residue (below) after chlorination. f) Element mass ratio in cathode waste and black mass before and after FJH-ClO treatment. g) Elemental content (blue) and yield (red) of Li, Co, and graphite after separation from black mass. All error bars in (g) represent the standard deviation, where N=3.

from black mass (Figure 3a). Typically, black mass is composed of a mixture of cathodes, anodes, binders, and electrolyte residues. In our study, we manually mixed LCO active material scraped from spent LCO cathodes with graphite powder to simulate black mass. The LCO cathode waste (Figure 3b, top) was recovered from used commercial 18650 cylindrical cells (LGDAHB21865-P308K034A3) sourced from a local recycler in Houston. After scraping the LCO active material from the Al foil and annealing it at  $\approx$ 600 °C to remove the polyvinylidene fluoride (PVDF) binder (Figure \$23, Supporting Information), it was mixed with graphite at a mass ratio of 2:1 to form simulated black mass (Figure 3b, bottom). When only the cathode waste is considered, Li can be separated and recovered from the spent LCO cathode with a Li content as low as 4.5% (Figure S24, Supporting Information), achieving a Li purity of 97.0% and a recovery rate of 90.6% through the FJH-CIO and water leaching process (Figure S25, Supporting Information). In contrast, when recovering Li from

black mass, the reaction is essentially referred to as carbochlorination due to the presence of graphite. This carbochlorination is also effective for both Li and Co. See Figure \$26 (Supporting Information) for the thermodynamics of carbochlorination. At the same temperature used for the chlorination of LCO powder, the carbochlorination of LCO black mass enables a fast reaction rate, completing in 30 s. In this process, Li and Co are chlorinated and sublimed into the volatile phase, while graphite remains on the carbon paper (Figures S27-S29, Supporting Information). XRD patterns show that the starting material contains graphite and LiCoO<sub>2</sub> (Figure 3c, bottom), the volatile phase consists mainly of CoCl<sub>2</sub>•6H<sub>2</sub>O and LiCl•H<sub>2</sub>O after the carbochlorination and air exposure (Figure 3c, middle), while only graphite remains in the residue (Figure 3c, top). SEM-EDS elemental analysis reveals a strong Cl signal in the chlorinated sample, confirming the presence of chlorides (Figure 3d, middle), whereas the residue shows only carbon signals, indicating that metals were well-chlorinated

om/doi/10.1002/adma.2025/17293 by James M Tour - Rice University, Wiley Online Library on [15/11/2025]. See the Terms and Conditions (https://onlinelibrary.wiley.com/terms-and-conditions) on Wiley Online Library for rules of use; OA articles are governed by the applicable Creative Commons

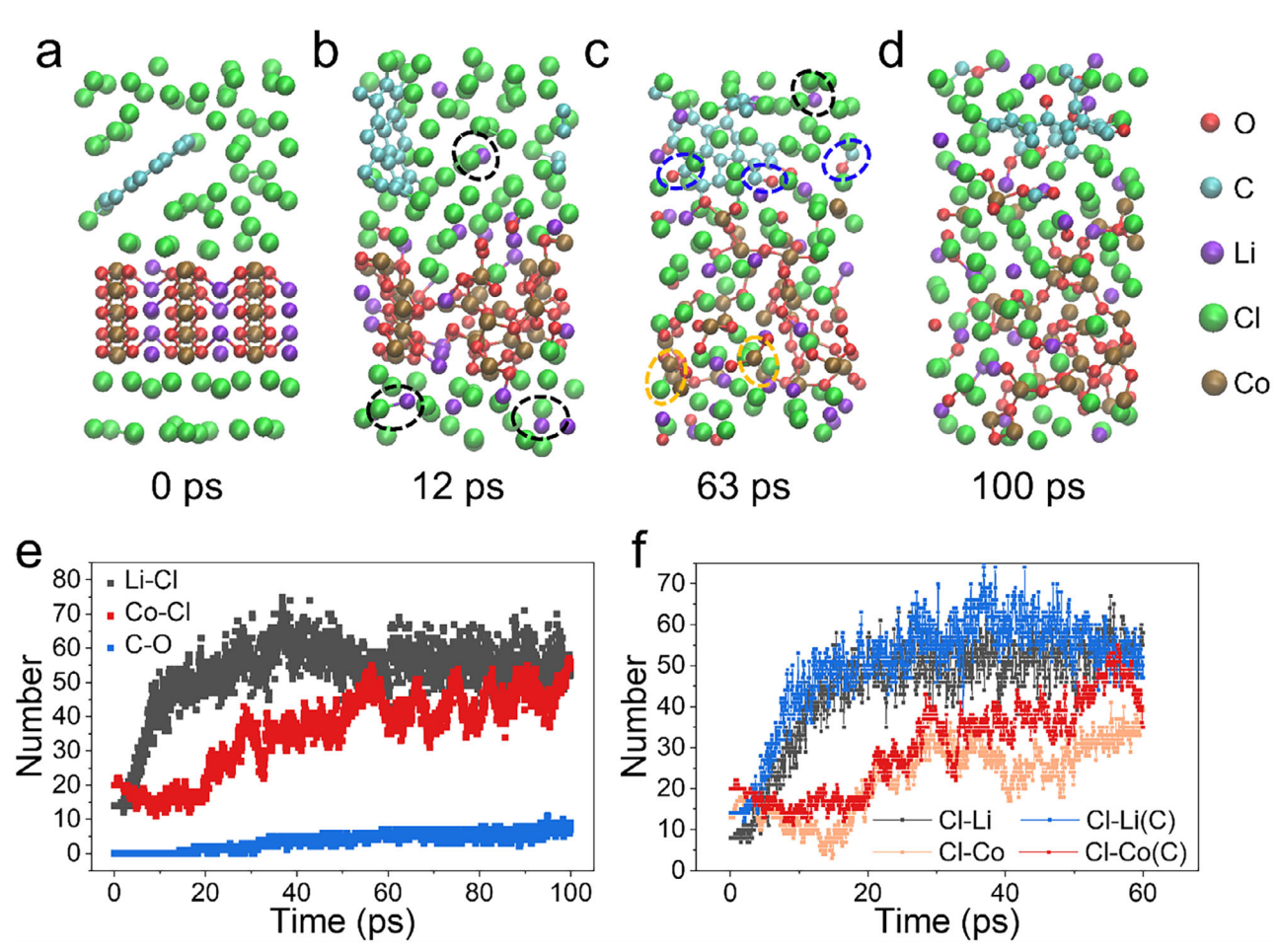


Figure 4. Molecular dynamics (MD) simulations of the carbochlorination of LCO-based black mass. The simulation time is 100 ps for LCO. Bonding evolution from the a) initial state to b) 12 ps, c) 63 ps, and d) 100 ps, respectively. Red: O atoms; brown: Co atoms, ice-blue: C atoms; violet: Li atoms, green: Cl atoms. Black dashed circle: Li—Cl bond; yellow dashed circle: Co—Cl bond; blue dashed circle: C—O bond. e) Evolution of the number of Co—Cl, Li—Cl, and C—O bonds during the carbochlorination of LCO within 100 ps. f) Comparison of the number of Li—Cl and Co—Cl bonds in the chlorination and carbochlorination reactions of LCO.

and entered the volatile phase (Figure 3d, top). The Li 1s XPS spectrum indicates that in the black mass, Li mainly exists in metallic form within LCO, corresponding to a binding energy  $\approx$ 54.29 eV (Figure 3e, bottom). In contrast, in the volatile phase, Li exists as LiCl, causing the peak to shift to 56.36 eV, confirming the presence of Li<sup>+</sup> (Figure 3e, middle). No lithium signal is detected in the residue (Figure 3e, top), once again confirming efficient chlorination of all metals via the carbochlorination reaction. Similarly, all collected chlorides were subjected to annealing at 450 °C for 30 min. The enhancement of the O signal and the weakening of the Cl signal in the XPS spectra confirm that oxidation occurs (Figure S30, Supporting Information). Followed by water leaching, Co and Li were further separated. ICP results show that Li purity can be improved from 4.4% in black mass to 98.8% after the treatment protocol (Figure 3f). More importantly, using the chlorination-oxidation-water leaching strategy (Figure 3a), Li, Co, and graphite can be separately and efficiently recovered. The purity of Li reaches 98.8%, with a recovery rate of 92.2% (Figure \$31, Supporting Information); Co reaches 99.5% purity and 96.5% recovery; graphite shows 99.9% purity (ppb level metallic impurities, Figure S32, Supporting Information) with a recovery rate of 85%, as part of the graphite is consumed in the carbochlorination reaction (Figure 3g). Industrial black mass often contains a mixture of multiple cathode wastes rather than a single composition. For such complex mixtures, the combination of the FJH–ClO process with precisely controlled stepwise chlorination would enable the potential separation of different cathode metals according to their distinct chlorination temperature windows (Figure S33, Supporting Information).

## 5. Molecular Dynamics (MD) Simulations

To gain deeper insight into the carbothermal chlorination of LCO black mass, molecular dynamics (MD) simulations were employed to investigate the role of graphite in the chlorination process. **Figure 4a**—d illustrates the bonding evolution from the initial state to 10, 63, and 100 ps, respectively. Experimentally, 30 s of carbochlorination leads to the formation of LiCl and CoCl<sub>2</sub>; however, the simulations reveal a different sequence of reactions: Li is preferentially chlorinated before Co. At 12 ps (Figure 4b), Li

15214095, 0, Downloaded from https://advanced.onlinelibrary.wiley

com/doi/10.1002/adma.202517293 by James M Tour - Rice University , Wiley Online Library on [15/11/2025]. See the Terms and Conditions (https://onlinelibrary.wiley

on Wiley Online Library for rules of use; OA articles are governed by the applicable Creative Commons

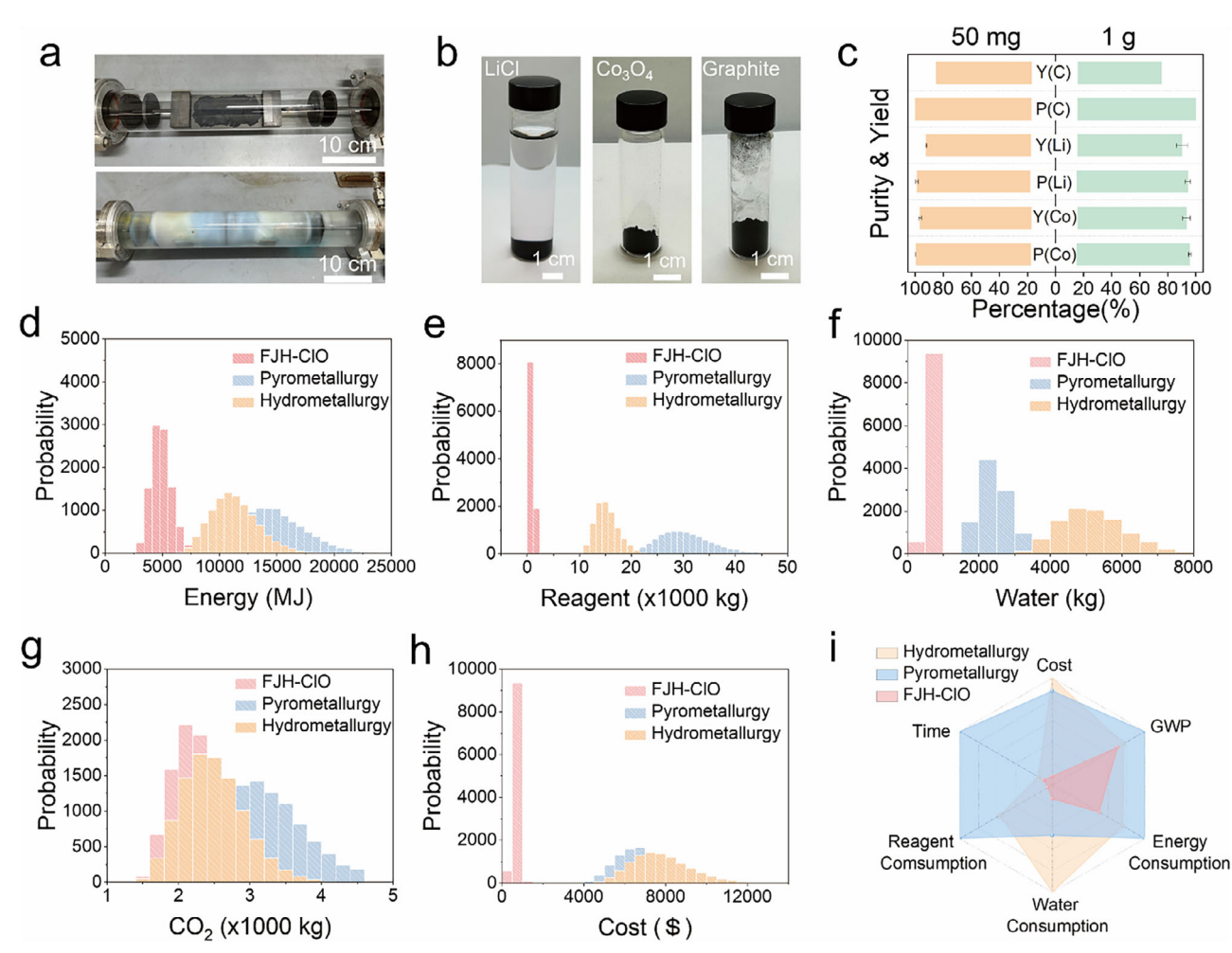


Figure 5. Scalability of Li separation by FJH-ClO and LCA/TEA results for FJH-ClO, hydrometallurgy, and pyrometallurgy separation processes. a) Photographs of the 3 inch quartz tube before (top) and after (bottom) the reaction. b) Separated LiCl solution,  $Co_3O_4$  powder, and graphite powder after FJH-ClO and water leaching treatment. c) Comparison of the purity (P) and yield (Y) of graphite (C), Li, and Co after separating from 50 mg of black mass in the 1 inch setup and 1 g of black mass in the 3 inch setup. All error bars in (c) represent the standard deviation, where N=3. Probability histograms are plotted for the d) energy consumption in MJ, e) reagents consumption in kg, f) water consumption in kg, g) GWP in kg  $CO_2$  eq, and h) processing cost in US dollars necessary to produce 1 tonne of Li from black mass. The higher the probability and the narrower the plotted histogram, the more accurate the prediction. i) A radar plot simultaneously comparing the six key variables associated with the FJH-ClO, hydrometallurgy, and pyrometallurgy processes to separate 1 tonne of Li. All axes in the radar plot are normalized to a maximum value of 5, corresponding to 100% for each metric. Each concentric ring on the plot thus represents a 20% increment.

atoms located in the interlayer region of LCO are more susceptible to departing from the LCO framework and being chlorinated owing to their higher mobility, lower binding energy, and weaker electrostatic interaction with the lattice compared with Co. This trend is further corroborated by Figure 4e, which shows that during the first 40 ps, Cl predominantly bonds with Li, and the number of Li-Cl bonds continues to increase over time. As the reaction progresses, Cl<sub>2</sub> begins to penetrate the lattice and bond with Co. However, the presence of stable Co-O bonds hinders the chlorination rate of Co. In contrast, when C (graphite) is involved, the formation of C-O bonds coincides with the emergence of Co-Cl bonds (Figure 4c), indicating that carbon facilitates the cleavage of Co-O bonds and thereby accelerates chlorination of Co. A direct comparison reveals that, under carbothermal conditions, the number of Li-Cl bonds increases only slightly relative to the pure chlorination reaction, whereas the number of Co-Cl

bonds increases significantly, confirming the promoting effect of carbon. These findings are consistent with the Gibbs free energy trends obtained from HSC calculations (Figure 1f; Figure S26, Supporting Information). It is also noteworthy that, due to the closed-system nature of the MD simulation, the limited Cl supply and the inability of CO to escape, there is a dynamic equilibrium between Li—Cl and Co—Cl bond populations at 100 ps (Figure 4d).

# 6. Scalability of the FJH-ClO Process

By enlarging the quartz tube, carbon paper, and associated components, the reaction system can be scaled up from 50 mg in a 1 inch tube setup to a 3 inch tube setup (**Figure 5**a, top; Figure S34, Supporting Information), enabling separation experiments with at least 1 g of black mass powders (2.54 cm = 1 inch; quartz

www.advancedsciencenews.com

ADVANCED MATERIALS

www.advmat.de

15214055, O. Downloaded from https://advanced.onlinelibrays.wiley.com/doi/10.102/adma.2025/7293 by James M Tour - Ric University, Wiley Online Library on [15/11/2025]. See the Terms and Conditions (https://onlinelibrary.wiley.com/erms-and-conditions) on Wiley Online Library for rules of use; OA articles are governed by the applicable Creative Commons Licenses are Conditions on Wiley Online Library for rules of use; OA articles are governed by the applicable Creative Commons Licenses are Conditions on Wiley Online Library for rules of use; OA articles are governed by the applicable Creative Commons Licenses are conditions on Wiley Online Library for rules of use; OA articles are governed by the applicable Creative Commons Licenses are conditions of the Creative Commons Licenses are conditions on Wiley Online Library for rules of use; OA articles are governed by the applicable Creative Commons Licenses are conditions of the Creati

tubes are sold in inches for the outer diameter). In this process, a mixture of LCO cathode waste powder and graphite at a mass ratio of 2:1 (total mass of 1 g) is uniformly spread onto a piece of carbon paper measuring 15 cm  $\times$  5 cm (Figure 5a, top). After reacting at 1460 °C for 3 min, Li and Co are chlorinated, and LiCl and CoCl<sub>2</sub> are condensed on the surface of the 3 inch quartz tube (Figure 5a, below). Similarly, after calcining the collected powder at 450 °C for 30 min, the powder is immersed in water, where LiCl dissolves while Co<sub>3</sub>O<sub>4</sub> does not (Figure 5b, left). After centrifugation and filtration, Co<sub>3</sub>O<sub>4</sub> is obtained as a solid (Figure 5b, middle; Figure \$35, Supporting Information). The remaining solid after the chlorination reaction is graphite, whose structural quality shows little change compared with the pristine graphite, indicating its strong potential for direct reuse in battery anodes (Figure 5b, right; Figure S36, Supporting Information). Compared with the separation performance in the 1 inch 50 mg setup, the scaled-up 1 g reaction also yields high-purity products (Table S5, Supporting Information), with Li purity reaching 94.2% and a yield of 90.1%, and Co purity reaching 95.6% with a yield of 93.2%. Due to the longer reaction time, more carbon participates in the carbochlorination reaction, resulting in a graphite recovery rate of 75.5%. The Li and Co residues in the recovered graphite are only 10 and 13 ppm, respectively, giving it a purity of ≈99.9% (Figure \$37, Supporting Information). Although FJH– ClO delivers high separation efficiency, a trade-off is the partial consumption and mild degradation of graphite during carbochlorination. In future work, optimizing the carbon-to-chlorine ratio and recycling the CO generated during the process will be important for improving carbon utilization and environmental sustainability. Overall, these results confirm the scalability of the reaction process. For industrial applications, a proportional scale-up of the reaction setup can enable large-scale separation. [49,50]

# 7. Life Cycle Assessment (LCA), Technoeconomic Analysis (TEA), and Environmental Considerations

Monte Carlo LCA and TEA calculations were employed to compare the predicted costs and environmental impact between the FJH-ClO process and the two most common battery waste treatment processes, hydrometallurgical and pyrometallurgical methods.<sup>[21-35]</sup> The Monte Carlo analysis allows for the comprehensive evaluation of uncertainties and variabilities in critical economic and technical parameters. By running 10 000 iterations at a 95% confidence interval for all inputs and outputs, this technique can provide a probabilistic Gaussian distribution of costs, materials consumed, and waste produced. This approach is necessary when many variables, such as energy consumption, emissions, and materials demand and usage, can vary widely. Additional details on the LCA and TEA analysis can be found in the Experimental Section and Text \$4 (Supporting Information), while the Monte Carlo LCA and TEA data for each process can be found in Tables S6-S9 and Datasets S1-S4 (Supporting Information).

The primary factors considered in the LCA and TEA were energy consumption, greenhouse gas emissions (GHG), specifically  $CO_2$ , as global warming potential (GWP), water and acid consumption, and processing cost (Dataset S1, Supporting Information). These factors were chosen since they contribute the most to materials cost, consumption, waste produced, and overall process costs. Processing 1 tonne of black mass produces 62–

71 kg of Li for the FJH-ClO and industrial methods. Compared to the hydrometallurgical process to produce 1 tonne of Li, the LCA shows that FJH-ClO can reduce the energy consumption by 34% from  $\approx$ 11 099 to  $\approx$ 7348 MJ (Figure 5d), reagent consumption by 92% from  $\approx$ 20 128 to  $\approx$ 1696 kg (Figure 5e), water consumption by 87% from  $\approx$ 5118 to  $\approx$ 663 kg (Figure 5f), operation time by 38% from  $\approx$ 21 to  $\approx$ 13 h (Figure S34, Supporting Information), and eliminate the use of acids during the separation process. The GWP difference is 8% for FJH-ClO, with a difference of  $\approx$ 2489 to  $\approx$ 2277 kg CO $_2$  (Figure 5g). The major contribution to the GWP for FJH-ClO is the use of carbon paper on a large scale during FJH-Cl $_2$ . The TEA also shows a reduction in operating costs of up to 92% from  $\approx$ \$7670 to  $\approx$ \$624 per tonne of Li isolated from black mass (Figure 5h).

Compared to the industrial pyrometallurgical process to produce 1 tonne of Li, the LCA shows that FJH-ClO can reduce the energy consumption by 49% from ≈14,540 to ≈7,348 MJ (Figure 5d), GHG emissions through the GWP by 29% from ≈3223 to ≈2277 kg CO<sub>2</sub> (Figure 5g), reagent consumption by 95% from  $\approx$ 35 551 to  $\approx$ 1696 kg (Figure 5e), water consumption by 72% from  $\approx$ 2400 to  $\approx$ 663 kg (Figure 5f), operation time by 91% from  $\approx$ 137 to  $\approx$ 13 h (Figure S38, Supporting Information). The TEA also shows a reduction in operating costs of up to 91% from ≈\$6734 to ≈\$624 per tonne of Li isolated from black mass (Figure 5h). GWP, reagent, and water consumption, and operation costs account for industrial scenarios where  $\approx$ 95% of excess reagents, such as Cl<sub>2</sub>, acid, base, and water, can be recycled from the original material to minimize the produced slag and waste. Figure 5i compares six key environmental and economic metrics between the FJH-ClO, hydrometallurgy, and pyrometallurgy processes: cost, reagent consumption (acid, base, Cl2, etc.), water use, operation time, energy consumption, and CO<sub>2</sub> emissions (Table S6, Supporting Information). Each axis of the radar plot represents one of these quantitative variables, and all axes in the radar plot are normalized to a maximum value of 5, corresponding to 100% for each metric. Each concentric ring on the plot thus represents a 20% increment. As evident from the radar chart, our method offers clear advantages over traditional pyrometallurgical and hydrometallurgical processes, particularly in terms of environmental impact, energy efficiency, economic cost, and chemical consumption. These benefits highlight its potential to play a critical role in addressing the challenges posed by the growing scarcity of lithium resources.

#### 8. Conclusion

In summary, we have developed a scalable and environmentally friendly strategy based on FJH-ClO for the holistic recovery of valuable components from spent lithium-ion batteries. The FJH-ClO process enables the selective transformation of cathode metals into chlorides and oxides, allowing for the efficient separation of Li from transition metals by leveraging their differences in water solubility. The method demonstrates excellent performance across various cathode materials, including LCO, LFP, and LMFP, and is further validated on realistic black mass. Gramscale experiments confirm the feasibility of scaling up the process while maintaining high recovery efficiency and purity. In addition, life-cycle assessment (LCA) and technoeconomic analysis (TEA) reveal that FJH-ClO dramatically reduces energy and

15214095, 0, Downloaded from https://advanced.onlinelibrary.wiley.com/doi/10.1002/adma.202517293 by James M Tour - Rice University, Wiley Online Library on [15/11/2025]. See the Terms and Conditions (https://onlinelibrary.wiley.

-and-conditions) on Wiley Online Library for rules of use; OA articles are governed by the applicable Creative Commons

water consumption, greenhouse gas emissions, and operating costs compared to conventional pyrometallurgical and hydrometallurgical processes. These results collectively highlight the potential of FJH-ClO as a sustainable, cost-effective, and industrially viable solution for battery recycling and resource recovery.

# 9. Experimental Section

Materials: The carbon paper was purchased from FuelCellStore (Toray Carbon Paper 060). The LiCoO2 (LCO, 442704-100G) and LiFePO4 (LFP, 759546-5G) were purchased from Sigma-Aldrich. LiMnFePO<sub>4</sub> (LMFP, 29023C2-500G) was purchased from MSE Supplies. The spent LCO cathode was obtained from used commercial 18650-cylinder cells (LGDAHB21865-P308K034A3) by a local recycler, Greater Texas Metal Recycling in Houston, Texas. The black mass is provided by Austin Elements, Houston, Texas. The standard solutions for ICP-MS tests included lithium standard (998  $\pm$  4 mg L<sup>-1</sup>, 12292-100ML), cobalt standard (1000  $\pm$  2 mg L<sup>-1</sup>, 30329-100ML-F), manganese standard (1003  $\pm$  5 mg L<sup>-1</sup>, 74128-100ML), and iron standard (1001  $\pm$  2 mg L<sup>-1</sup>, 43149-100ML-F), all of which were purchased from Millipore Sigma. The nitric acid (HNO<sub>3</sub>, 67-70 wt%, TraceMetalTM Grade, Fisher Chemical), hydrochloric acid (HCl, 37 wt%. 99.99%, trace metal basis, Millipore Sigma), and ultrapure water (Millipore Sigma, ACS reagent for ultra-trace analysis) were used for sample digestion. A Cl<sub>2</sub> cylinder (Airgas, 99.5%, 15 Lbs) was used to supply the Cl<sub>2</sub>. Argon gas (Airgas, 99.99%) was used to purge the system to remove moisture and air in the reaction chamber prior to the introduction of Cl<sub>2</sub>. The power supply is a direct current power supply (ZHAOXIN KXN-3060D, Electronics Co., LTD.) While the DCPS dial settings correspond to increasing current as they are turned higher, they are not an absolute current setting in amperes that matches the dial setting number, and this was calibrated (Table S2, Supporting Information).

Flash Joule Heating Chlorination System: The power source here is the DCPS, which is connected to the carbon paper via graphite rods and graphite blocks. Micro-Epsilon thermometer, CTM-3SF75H2-C and CTRM-1H1SF100-C3, was used to monitor the temperature of the carbon paper. The former tests the temperature range between 200 and 1500 °C, and the latter tests the temperature range between 1500 and 3000 °C. 30 mg samples (cathode powders or black mass) are spread evenly on the surface of carbon paper in a quartz tube and sealed at the ends of the tube with electrodes, an inlet chlorine gas line, and an outlet volatile gas line for unreacted chlorine. The quartz tube is conventionally 1 inch in outer diameter and 20 cm long. The size of carbon paper is  $2 \times 6$  cm, and the resistance is 0.8–1.0  $\Omega.$  Carbon felts and glass wool were used to lightly restrict the outlet of the quartz tube for better collection of volatiles. For safety considerations, a Cl<sub>2</sub> buffer tank was placed upstream of the reactor to avoid maintaining the main cylinder valve open continuously. This design limits gas discharge risk under abnormal conditions. The gas delivery line was constructed from stainless steel and sealed with a CGA-180 fitting and PTFE O-ring. The outlet gases were directed through two neutralization traps: the first packed with solid NaOH, and the second an aqueous NaOH absorber, to remove unreacted chlorine. All operations were conducted within a ventilated hood. Cl<sub>2</sub> in the final exhaust gas was not detectable (Figure S39, Supporting Information) by gas chromatography. In large-scale industrial applications, Cl<sub>2</sub> can also be properly recovered and reused; the ideal process would utilize a closed-loop condenser system.<sup>[51,52]</sup>

Characterization: XRD was performed by the Rigaku SmartLab system with filtered Cu Kα radiation ( $\lambda=1.5406$  Å). Raman spectra were acquired using a Renishaw Raman microscope (laser wavelength of 532 nm, laser power of 5 mW, 50x lens). SEM images were obtained using a FEI Quanta 400 ESEM FEG system at 20 kV. EDS spectra and maps were acquired using the same system equipped with an EDS detector. XPS was conducted using a PHI Quantera XPS system at a base pressure of  $5 \times 10^{-9}$  Torr. Elemental spectra were obtained with a step size of 0.1 eV with a pass energy of 26 eV. All the XPS spectra were calibrated using the standard C 1s peak at 284.8 eV. ICP-MS was performed by Perkin Elmer Nexion 2000B ICP-MS.

Molecular Dynamics (MD) Simulations: The Density Functional Theory (DFT) method<sup>[53]</sup> as implemented in the Vienna Ab-initio Simulation Package (VASP)<sup>[54]</sup> is used for molecular dynamics (MD) simulation of the chlorination and carbochlorination of LCO. A plane wave expansion up to 400 eV is employed in combination with an all-electron-like projector augmented wave (PAW) potential.<sup>[55]</sup> Exchange-correlation is treated within the generalized gradient approximation (GGA) using the functional parameterized by Perdew–Burke–Ernzerhof.<sup>[56]</sup> A periodic boundary condition is applied to the unit cell (or supercell) in all three dimensions. According to the size of the unit cell, the convergence of total energy is achieved with respect to k-points sampling for the Brillouin zone integration over Monkhorst–Pack type mesh.<sup>[57]</sup>

For MD simulation of the reaction of LCO with Cl molecules, a 5-atomic-layer (6 Å thick) LCO, along with a 20 Å vacuum slab, in which Cl<sub>2</sub> molecules and fragmented graphene containing 24 C atoms are incorporated. The density of the Cl<sub>2</sub> molecules is 15 Cl<sub>2</sub> nm $^{-3}$ . The average temperature of the MD simulation is set at 2000 K with a 500 K amplitude of oscillation throughout the 100 ps MD time scale. Three types of bonds are counted over the MD process with the cut-off length 2.7 Å for both Li—Cl and Co—Cl bonds, and 1.3 Å for Co—O bonds.

LCA and TEA: The LCA and TEA were performed using the life cycle inventory (LCI) from the European reference Life Cycle Database (ELCD) with the Centrum voor Milieukunde Leiden-Impact Assessment (CML-IA) baseline impact assessment in the OpenLCA software. [58] If not available in the ELCD database, LCI data were cited from the representative literature. As a preliminary "Class 4" estimate, 10 000 iterations of the Monte-Carlo simulations were performed for all processes at a 70% confidence interval (± 30% triangular distribution) for every analyzed variable according to the Association for the Advancement of Cost Estimating International (AACE International). [59] The triangular distribution limits randomly generated Monte Carlo values to specific minimum and maximum values. Distributions with large standard deviations, such as those provided, can generate imaginary values in the OpenLCA software, which can average the distribution to 0, thus generating a false distribution. This is also why an iteration value of 10 000 was chosen, since the triangular distribution will become approximately Gaussian after sufficient iterations of the Monte Carlo simulations. This non-amortized operating expense (OpEx) analysis assessed the necessary inputs to produce 1 tonne of Li from the FJH-Cl<sub>2</sub>, hydrometallurgy, and pyrometallurgy processes using various battery waste inputs, including black mass, LFP, LMFP, and LCO cathode waste. The TEA analysis does not account for capital expenses (CapEX). The OpenLCA software was used to calculate the TEA OpEx for each process to recycle 1 tonne of Li from black mass battery waste. This is done by assigning the TEA values found from Dataset 4 to the input material for each process, where the software then performs the Monte Carlo simulation for each process to assess the OpEx based on the input material values and their cost references.

The data used to simulate the battery recycling hydrometallurgy and pyrometallurgy processes were collected from the literature to compare them with experimental variables for the FJH-Cl<sub>2</sub> process. Data analysis from Monte–Carlo simulations was performed with Microsoft Excel and Origin to plot the histograms and radar plots. The input and output materials for both processes are available in Tables S7–S9 and Datasets S1–S4 (Supporting Information).

# **Supporting Information**

Supporting Information is available from the Wiley Online Library or from the author.

# **Acknowledgements**

The authors acknowledge the use of ChatGPT and Grammarly to rephrase and correct spelling and grammar errors and generate some conceptual illustrations for this work. The authors thank Dr. Bo Chen of Rice University for helpful input with the XPS results and Dr. Tanguy Terlier for developing ICP-MS methods. The funding of the research was provided by the

15214095, 0, Downloaded from https://advanced.onlinelibrary.wiley.com/doi/10.1002/adma.202517293 by James M Tour - Rice University , Wiley Online Library on [15/11/2025]. See the Terms and Conditions (https://onlinelibrary.wiley.

and-conditions) on Wiley Online Library for rules of use; OA articles are governed by the applicable Creative Commons

Defense Advanced Research Projects Agency (HR00112290122, J.M.T.), the Air Force Office of Scientific Research (FA9550-22-1-0526, J.M.T.), and the U.S. Army Corps of Engineers, ERDC (W912HZ-21-2-0050, J.M.T., B.I.Y., Y.Z.). Computer resources were provided through the DOE's NERSC award (BES-ERCAP0027822, B.I.Y.). The characterization equipment used in this project is partly from the Shared Equipment Authority (SEA) at Rice University. The authors also thank the black mass supplier, Austin Elements, Houston, Texas.

## **Conflict of Interest**

Rice University owns intellectual property on the separation of metals from waste and ores using flash Joule heating with or without concomitant chlorination. Much of this intellectual property has been licensed to a company in which J.M.T. is a shareholder, but he is not an employee, officer, or director in that company. Conflicts of interest are mitigated through disclosure to and compliance with the Rice University Office of Sponsored Programs and Research Compliance. The authors declare no other competing interests

## **Author Contributions**

S.C.X. and J.M.T. conceived the idea. S.C.X. conducted the experiments with the help of J.S., Q.M.L., J.S., H.X.Y., K.W.Y., S.H.C., K.S., R.A.N., C.K., B.W.L., K.J., C.T., and S.C.X. conducted all the characterization and analysis. J.S. conducted the technoeconomic analysis and life-cycle assessment and analyzed the results. S.C.X. and J.M.T. wrote the manuscript. All aspects of the research were overseen by J.M.T. All authors have discussed the results and given approval to the final version of the manuscript.

# **Data Availability Statement**

The data that support the findings of this study are openly available in Zenodo at https://doi.org/10.5281/zenodo.17039076, reference number 1.

## **Keywords**

black mass, chlorination, flash Joule heating, metal separation, spent battery  $% \left( 1\right) =\left( 1\right) \left( 1\right) \left($ 

Received: September 3, 2025 Revised: October 29, 2025 Published online:

- X. Ma, Z. Meng, M. Bellonia, J. Spangenberger, G. Harper, E. Gratz,
  E. Olivetti, R. Arsenault, Y. Wang, Nat. Rev. Clean Technol. 2025, 1, 75.
- [2] G. Harper, R. Sommerville, E. Kendrick, L. Driscoll, P. Slater, R. Stolkin, A. Walton, P. Christensen, O. Heidrich, S. Lambert, A. Abbott, K. Ryder, L. Gaines, P. Anderson, *Nature* 2019, 575, 75.
- [3] X. Zhang, L. Li, E. Fan, Q. Xue, Y. Bian, F. Wu, R. Chen, Chem. Soc. Rev. 2018, 47, 7239.
- [4] H. Baea, Y. Kim, Mater. Adv 2021, 2, 3234.
- [5] H. Ji, J. Wang, J. Ma, H. M. Cheng, G. Zhou, Chem. Soc. Rev. 2023, 52, 8194.
- [6] J. Wang, J. Ma, Z. Zhuang, Z. Liang, K. Jia, G. Ji, G. Zhou, H. M. Cheng, Chem. Rev. 2024, 124, 2839.
- [7] E. Fan, L. Li, Z. Wang, J. Lin, Y. Huang, Y. Yao, R. Chen, F. Wu, Chem. Rev. 2020, 120, 7020.

- [8] M. P. Jonas Neumann, M. Meeus, J. D. Gamarra, R. Younesi, M. Winter, S. Nowak, Adv. Energy Mater. 2022, 12, 2102917.
- [9] R. E. B. Zachary, J. Baum, X. Yu, J. Ma, ACS Energy Lett. 2022, 7, 712.
- [10] Z. Lai, J. Long, Y. Lu, F. Luo, L. Zeng, W. Lai, Y. Li, Q. Qian, Q. Chen, K. Zhang, Z. Yan, J. Chen, Adv. Energy Mater. 2025, 15, 2501009.
- [11] A. Tankou, G. Bieker, D. Hall, Scaling Up Reuse and Recycling of Electric Vehicle Batteries, The International Council on Clean Transportation, Washington, D.C., USA 2023.
- [12] National Blueprint for Lithium Batteries 2021–2030, https://www.energy.gov (accessed: July 2025).
- [13] E. A. Olivetti, G. Ceder, G. G. Gaustad, X. Fu, Joule 2017, 1, 229.
- [14] P. Li, S. Luo, Y. Lin, J. Xiao, X. Xia, X. Liu, L. Wang, X. He, Chem. Soc. Rev. 2024, 53, 11967.
- [15] Y. S. Tang, Y. B. Yang, M. C. Pan, M. C. Xiao, G. S. Jiang, Z. Tan, Y. Xue, J. X. Wu, X. G. Zhang, W. Zhang, D. A. Pan, Adv. Funct. Mater. 2025, 13322
- [16] J. V. Velázquez-Martínez Omar, A. Santasalo-Aarnio, M. Reuter, R. Serna-Guerrero, Batteries 2019, 5, 68.
- [17] X. Wu, Y. Liu, J. Wang, Y. Tan, Z. Liang, G. Zhou, Adv. Mater. 2024, 36, 2403818.
- [18] Y. L. Jingxiu Wang, R. Zeng, S. Zhang, K. Davey, J. Mao, Z. Guo, Energy Environ. Sci. 2024, 17, 867.
- [19] Y. Mei, R. Chen, Z. Shao, W. Qin, L. Xu, L. Liu, J. Zhou, J. Hu, H. Hou, L. Yuan, J. Yang, Adv. Funct. Mater. 2025, 35, 2507185.
- [20] X. Lv, J. Lin, X. Sun, Q. Huang, X. Zhang, T. Yu, E. Fan, Y. Ye, R. Chen, F. Wu, L. Li, Adv. Mater. 2025, 37, 2503398.
- [21] X. Chen, Y. Chen, T. Zhou, D. Liu, H. Hu, S. Fan, Waste Manag. 2015, 38, 349.
- [22] Y. Cao, J. Li, H. Ji, X. Wei, G. Zhou, H. M. Cheng, Energy Storage Mater. 2024, 70, 103475.
- [23] L. Li, E. Fan, Y. Guan, X. Zhang, Q. Xue, L. Wei, F. Wu, R. Chen, ACS Sustainable Chem. Eng. 2017, 5, 5224.
- [24] S. P. Barik, G. Prabaharan, L. Kumar, J. Clean. Prod. 2017, 147, 37.
- [25] W.-S. Chen, H.-J. Ho, Metals 2018, 8, 321.
- [26] Y. Fu, Y. He, L. Qu, Y. Feng, J. Li, J. Liu, G. Zhang, W. Xie, Waste Manag 2019 88 191
- [27] P. Yadav, C. J. Jie, S. Tan, M. Srinivasan, J. Hazard Mater. 2020, 399, 123068.
- [28] L. Yu, Y. Bai, R. Essehli, A. Bisht, I. Belharouak, Energy Storage Mater. 2023, 63, 103025.
- [29] J. Yu, Y. Liu, J. Li, Nat. Commun. 2025, 16, 2440.
- [30] J. Xiao, J. Li, Z. Xu, Environ. Sci. Technol. 2017, 51, 11960.
- [31] J. Lin, C. Liu, H. Cao, R. Chen, Y. Yang, L. Li, Z. Sun, Green Chem. 2019, 21, 5904.
- [32] J. Lin, L. Li, E. Fan, C. Liu, X. Zhang, H. Cao, Z. Sun, R. Chen, ACS Appl. Mater. Interfaces 2020, 12, 18482.
- [33] M. Zhou, B. Li, J. Li, Z. Xu, ACS EST Engg. 2021, 1, 1369.
- [34] X. Hu, E. Mousa, Y. Tian, G. Ye, J. Power Sources 2021, 483, 228936.
- [35] A. T. Montoya, Z. Yang, E. U. Dahl, K. Z. Pupek, B. Polzin, A. Dunlop, J. T. Vaughey, ACS Sustainable Chem. Eng. 2022, 10, 13319.
- [36] E. Nieto-Arango, J. J. Sánchez-Rojas, J. F. Palacios, D. Hernández-Pardo, D. Perez-Acevedo, P. Delvasto, Clean Technologies and Environmental Policy 2023, 26, 307.
- [37] Z. L. W. Wang, Z. Zhu, Y. Ma, K. Zhang, Y. Meng, T. Ahmad, N. Ali Khan, Q. Peng, Z. Xie, Z. Zhang, W. Chen, *Nat. Sustain.* 2025, 8, 287.
- [38] S. Li, X. Wu, Y. Jiang, T. Zhou, Y. Zhao, X. Chen, Waste Manag 2021, 136. 18.
- [39] L. Yang, Z. Gao, T. Liu, M. Huang, G. Liu, Y. Feng, P. Shao, X. Luo, Environ. Sci. Technol. 2023, 57, 4591.
- [40] M. A. Kasri, M. Z. Mohd Halizan, I. Harun, F. I. Bahrudin, N. Daud, M. F. Aizamddin, S. N. Amira Shaffee, N. A. Rahman, S. A. Shafiee, M. M. Mahat, RSC Adv. 2024, 14, 15515.
- [41] Z. Fang, P. Zhu, X. Zhang, Y. Feng, H. Wang, Nat. Chem. Eng. 2025, 2, 142.



www.advancedsciencenews.com

ADVANCED MATERIALS

www.advmat.de

15214095, 0, Downloaded from https://advanced.onlinelibrary.wiley.com/doi/10.1002/adma.202517293 by James M Tour - Rice University , Wiley Online Library on [15/11/2025]. See the Terms

and Conditions (https

of use; OA articles are governed by the applicable Creative Commons

- [42] Y. Yao, Z. Huang, P. Xie, S. D. Lacey, R. J. Jacob, H. Xie, F. Chen, A. Nie, T. Pu, M. Rehwoldt, D. Yu, M. R. Zachariah, C. Wang, R. Shahbazian-Yassar, J. Li, L. Hu, Science 2018, 359, 1489.
- [43] W. C. Wang, W. W. Ping, Q. Bai, H. Cui, R. Hensleigh, R. Wang, A. H. Brozena, Z. Xu, J. Dai, Y. Pei, C. Zheng, J. Gao, X. Wang, H. Wang, J.-C. Zhao, B. Yang, X. Zheng, J. Luo, Y. Mo, B. Dunn, L. Hu, Science 2020, 368, 521.
- [44] D. X. Luong, K. V. Bets, W. A. Algozeeb, M. G. Stanford, C. Kittrell, W. Chen, R. V. Salvatierra, M. Ren, E. A. McHugh, P. A. Advincula, Z. Wang, M. Bhatt, H. Guo, V. Mancevski, R. Shahsavari, B. I. Yakobson, J. M. Tour, *Nature* 2020, 577, 647.
- [45] W. Chen, R. V. Salvatierra, J. T. Li, C. Kittrell, J. L. Beckham, K. M. Wyss, N. La, P. E. Savas, C. Ge, P. A. Advincula, P. Scotland, L. Eddy, B. Deng, Z. Yuan, J. M. Tour, Adv. Mater. 2023, 35, 2207303.
- [46] H. Shang, W. Yang, Z. He, J. Luo, F. Yu, C. Jia, X. Zhu, ACS EST Engg. 2025, 5, 724.
- [47] W. Chen, J. Chen, K. V. Bets, R. V. Salvatierra, K. M. Wyss, G. Gao, C. H. Choi, B. Deng, X. Wang, J. T. Li, C. Kittrell, N. La, L. Eddy, P. Scotland, Y. i. Cheng, S. Xu, B. Li, M. B. Tomson, Y. Han, B. I. Yakobson, J. M. Tour, Sci. Adv. 2023, 9, adh5131.

- [48] B. Deng, S. Xu, L. Eddy, J. Shin, Y. Cheng, C. Kittrell, K. JeBailey, J. Sharp, L. Qian, S. Chen, J. M. Tour, Nat. Chem. Eng. 2024, 1, 627.
- [49] Universal Matter, https://www.universalmatter.com (accessed: August 2025).
- [50] Metallium, https://metalliuminc.com (accessed: August 2025).
- [51] T. F. O'Brien, T. V. Bommaraju, F. Hine, Handbook of Chlor-Alkali Technology, Springer US, Boston 2005.
- [52] K. A. Lokhandwala, Ind. Eng. Chem. Res. 1999, 38, 3606.
- [53] S. L. Dudarev, G. A. Botton, S. Y. Savrasov, C. J. Humphreys, A. P. Sutton, *Phys. Rev. B* 1998, 57, 1505.
- [54] G. Kresse, J. Furthmuller, Phys. Rev. B 1996, 54, 11169.
- [55] P. E. Blochl, Phys. Rev. B 1994, 50, 17953.
- [56] J. P. Perdew, K. Burke, M. Ernzerhof, Phys. Rev. Lett. 1996, 77, 3865.
- [57] H. J. Monkhorst, J. D. Pack, Phys. Rev. B 1976, 13, 5188.
- [58] OpenLCA Software, https://www.openlca.org (accessed: July 2024).
- [59] A.A.C.E. International Recommended Practice, Cost Estimate Classification System As applied in engineering, procurement, and construction for the building and general construction industries, https://www.scribd.com/document/636044812/Untitled (accessed: July 2024).